Progress In Electromagnetics Research, Vol. 105, 71–92, 2010

MODELLING OF RECONFIGURABLE TERAHERTZ INTEGRATED ARCHITECTURE (RETINA) SIW STRUCTURES

Y. Zhou and S. Lucyszyn

Optical and Semiconductor Devices Group
Department of EEE
Imperial College London
London, SW7 2AZ, United Kingdom

Abstract—This paper discusses for the first time the combined optoelectronic-electromagnetic modelling of a new technology that represents a paradigm shift in the way millimetre-wave and terahertz electronics can be implemented using the REconfigurable Terahertz INtegrated Architecture (RETINA) concept. Instead of having traditional metal-pipe rectangular waveguide structures with metal sidewalls, RETINA structures have photo-induced *virtual* sidewalls within a high resistivity silicon substrate. This new class of substrate integrated waveguide (SIW) technology allows individual components to be made tuneable and subsystems to be reconfigurable, by changing light source patterns. Detailed optoelectronic modelling strategies for the generation of *virtual* sidewalls and their electromagnetic interactions are presented in detail for the first time. It is found with double-sided illuminated RETINA structures that an insertion loss of $1.3\,\mathrm{dB}/\lambda_g$ at 300 GHz is predicted for the dominant TE_{10} mode and for a cavity resonator a Q-factor of 4 at 173 GHz is predicted for the TE_{101} mode. While predicted losses are currently greater than other non-tuneable/reconfigurable SIW technologies, there is a wide range of techniques that can be investigated to considerably improve their performance, while still allowing completely arbitrary topologies to be defined in the x-z plane and in real time. For this reason, it is believed that this technology could have a profound impact on the future of millimetre-wave and terahertz electronics. As a result, this paper could be of interest to research groups that have the specialised experimental resources to implement practical demonstrator exemplars.

Corresponding author: S. Lucyszyn (s.lucyszyn@imperial.ac.uk).

1. INTRODUCTION

The ability to control subsystem building blocks within a front-end architecture, by electronic/optical means, is important if the overall system is to be adaptive or requires multi-functionality. Techniques for achieving this are well established at microwave [1, 2], millimeter-wave [2] and optical frequencies. However, for circuits operating at upper-millimetre-wave and terahertz frequencies (e.g., *circa* 100 GHz to 3 THz) rectangular waveguides represent the only realistic form of guided-wave structure. Trying to realise and integrate tuneable/reconfigurable circuits (e.g., impedance matching networks, filters, directional couplers, phase shifters/delay lines, etc.) and even high-level switching functions at these frequencies is very challenging indeed.

Traditional methods for implementing upper-millimetre-wave and terahertz systems rely on conventional techniques, whereby physical components are used to create permanent structures. This tried and trusted philosophy can be prohibitively expensive if tuneable circuits need to be implemented and/or electronically reconfigurable architectures are required. Moreover, such techniques are not compatible with an integrated solution. The answer may require a paradigm shift in the way engineers realize their components, circuits and front-end subsystems.

The metal-pipe rectangular waveguide (MPRWG) is the most important guided-wave structures at these frequencies, because of its relatively low loss and high cross-talk isolation characteristics and, therefore, its ability to implement high performance components, circuits and front-end subsystems. Indeed, for these reasons, it is the waveguide of choice for non-tuneable/reconfigurable applications above *circa* 100 GHz and many diverse technologies exist to realize integrated forms of the MPRWG [3–11].

Understanding photo-induced (electron-hole pair) plasmas within a semiconductor is important for the development of solid-state device operation. Indeed, photoconductivity has been exploited as an effective means to control microwave signals for over three decades. Recently, an entirely new class of tuneable/reconfigurable substrate integrated waveguide (SIW) technology was proposed for terahertz applications [12], in which the sidewalls from traditional MPRWGs are replaced by photo-induced conducting sidewalls within a high-resistivity silicon (HRS) substrate. These conducting sidewalls are formed according to a light pattern projected onto the surface of the HRS, allowing tuneable structures and reconfigurable architectures to be implemented by real-time manipulation of light patterns in the x-

z plane. In principle, complete front-end subsystems and all their individual components can be made with photo-induced conducting sidewalls, although in practice it is more likely that just key walls would be spatially moved to facilitate tuneability and/or reconfigurability. The physics behind the proposed Reconfigurable Terahertz INtegrated Architecture (RETINA) concept will now be introduced in more detail.

The basic RETINA SIW concept has its *virtual* sidewalls created from regions made highly conductive by the photo-generation of free charged carriers (electrons and holes). Photoconductivity within semiconductors and other materials has been known and exploited for many decades [13]. Applications include: optical detectors [14], sub-picosecond switches [15, 16], optically-controlled microwave devices [17, 18] and experimental Bragg reflecting filters [19]. In all these cases, the photo-induced electro-hole pair plasma region is generally confined to the surface of the semiconductor. In contrast, with reference to Fig. 1, RETINA structures rely on the photo-induced plasma being extended from the top surface downwards towards the bottom surface of the semiconductor.

Figure 1 shows the cross-section of a basic RETINA SIW structure to create a *virtual* MPRWG. The top surface of the waveguide is made from a layer of transparent conductive oxide (TCO), e.g., indium tin oxide (ITO). TCO materials have a relatively low plasma frequency, which can make them transparent within the infrared (IR) part of the frequency spectrum. As a result, they exhibit low attenuation of light from a near-IR laser source, while providing good reflectivity at upper-millimetre-wave and terahertz frequencies.

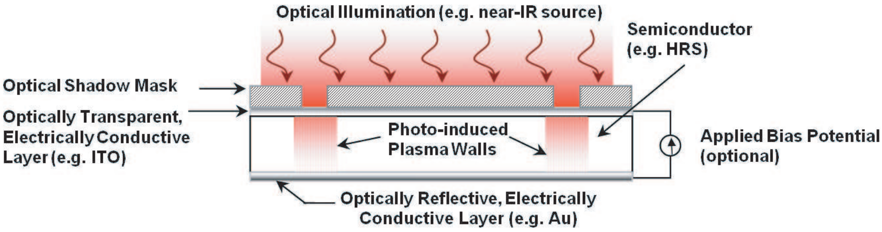

Figure 1. Simplified cross-sectional illustration of the basic RETINA SIW structure to create a *virtual* MPRWG using single-sided illumination.

Table 1. Definition of parameters with room temperature values [13, 14, 21–23].

Variable	**Description**	**Value**	**Unit**
A	Illumination area	–	μm^2
a	Internal MPRWG width cross-sectional dimension	285 for HRS	μm
b	Internal MPRWG height cross-sectional dimension	100 for HRS	μm
c	Speed of light in vacuum	2.99792458×10^8	$\text{m} \cdot \text{s}^{-1}$
D_a	Diffusion constant	54.3 for Si	$\text{cm}^2 \cdot \text{s}^{-1}$
e	Electron charge	1.60218×10^{-19}	C
E_g	Band gap energy	1.12 for Si	eV
f	Frequency	–	Hz
f_c	Cut-off frequency	154 for HRS	GHz
f_0	Operating frequency	300	GHz
h	Planck's constant	6.62617×10^{-34}	$\text{J} \cdot \text{s}$
I	Illumination optical power density	80	$\text{W} \cdot \text{cm}^{-2}$
k	Boltzmann constant	1.381×10^{-23}	$\text{J} \cdot \text{K}^{-1}$
L_a	Diffusion length for high-injection condition	73.5 for HRS	μm
$\overline{m}^*$	Average effective mass for both electrons and holes	2.91×10^{-31}	kg
n	Refractive index	3.42 for Si 1.96 for ITO	
N	Photo-induced carrier density for electrons or holes	–	cm^{-3}
$N(x)$	Photo-induced carrier concentration distribution in x direction	–	cm^{-3}
$N(y)$	Photo-induced carrier concentration distribution in y direction	–	cm^{-3}
ΔN_o	Photo-induced carrier density at the surface	3.7×10^{16}	cm^{-3}
P	Peak power of optical illumination	–	W

R	Surface power reflectivity	0.4 for Si	–
S_λ	Relative spectral response (photosensitivity) at λ_{opt}	0.6 for HRS	–
T	Absolute temperature	300	K
w	Beam width of uniform illumination	50	µm
a_λ	Radiation absorption coefficient at λ_{opt}	1,000 for HRS	cm^{-1}
$\sigma(x)$	Photoconductivity distribution in x direction	–	$\mathrm{S \cdot m^{-1}}$
$\Delta\sigma_o$	Photoconductivity at the surface	1,251 for HRS	$\mathrm{S \cdot m^{-1}}$
σ_o	Bulk dc conductivity	4.1×10^7 for gold 8.0×10^5 for ITO	$\mathrm{S \cdot m^{-1}}$
σ_D	Dark bulk dc conductivity (used in HFSS simulations)	1.25×10^{-4} for HRS	$\mathrm{S \cdot m^{-1}}$
σ_h	Empirical σ_m to obtain σ_{mh}	7,422 for HRS	$\mathrm{S \cdot m^{-1}}$
σ_m	Maximum bulk dc photoconductivity	–	$\mathrm{S \cdot m^{-1}}$
σ_{mh}	σ_m along the horizontal cut line at certain depth	2,921 for 30 µm depth for HRS	$\mathrm{S \cdot m^{-1}}$
σ_{mv}	σ_m along the vertical cut line at beam centre	3,271 for HRS	$\mathrm{S \cdot m^{-1}}$
σ_R	Bulk conductivity at angular frequency ω	–	$\mathrm{S \cdot m^{-1}}$
ε_o	Permittivity of free space	8.85×10^{-12}	$\mathrm{F \cdot m^{-1}}$
ε_r	Relative permittivity at angular frequency ω	–	–
ε_{ro}	Relative permittivity at dc	11.9 for HRS	–
$\varepsilon(\omega)$	Complex permittivity at angular frequency ω	–	$\mathrm{F \cdot m^{-1}}$
μ_n	Mobility of electron	1,500 for HRS	$\mathrm{cm^2 \cdot V^{-1} \cdot s^{-1}}$
μ_p	Mobility of hole	600 for HRS	$\mathrm{cm^2 \cdot V^{-1} \cdot s^{-1}}$
v_s	Surface recombination velocity	100 for Si	$\mathrm{cm \cdot s^{-1}}$
τ	Carrier scattering relaxation time	381 for HRS 27.5 for gold 12.6 for ITO	fs

τ_L	Photo-induced carrier lifetime	10^{-6} for HRS	s
ω	Angular frequency	–	$\mathrm{rad} \cdot \mathrm{s}^{-1}$
ω_p	Angular plasma frequency	–	$\mathrm{rad} \cdot \mathrm{s}^{-1}$
ω_τ	Angular scattering relaxation frequency	–	$\mathrm{rad} \cdot \mathrm{s}^{-1}$
λ_{o_HRS}	Unguided wavelength in HRS	293 at 300 GHz	µm
λ_{opt}	Optical illumination wavelength	808	nm
λ_g	Guided wavelength	342 at 300 GHz for HRS	µm
λ_c	Cut-off wavelength	570 for HRS	µm

Table 2. Typical properties of semiconductors at room temperature [13, 14, 21–23].

Material	$\tau_L(s)$	E_g (eV)	μ ($\mathrm{cm}^2\mathrm{V}^{-1}\mathrm{s}^{-1}$)		σ_D (S/cm)	σ_m (S/cm)
			μ_n	μ_p		
HRS	10^{-6}–10^{-4}	1.1	1,500	600	10^{-6}–10^{-3}	$> 1,000$
Ge	10^{-4}	0.67	3,900	1,800	10^{-2}	> 600
GaAs	10^{-7}	1.43	8,500	400	10^{-2}	> 100
CdSe	10^{-4}	1.7	800	30	10^{-7}	2.77
InSb	10^{-7}	0.18	78,000	1,700	100	8,900
a-Si:H	–	0.7–0.8	1	0.02	10^{-9}–10^{-8}	10^{-3}–10^{-2}

2. PHOTO-INDUCED PLASMA

2.1. Material Selection

Photoconductivity is the increase in the electrical conductivity of a material caused by incident electromagnetic radiation [13]. In theory, a single photon can generate an electron-hole pair, provided its energy exceeds the band gap energy (E_g) of the material. In conjunction with Table 1, Table 2 gives a comparative list of basic properties for conventional semiconductors. From Table 2, it can be seen that HRS can provide a high photoconductivity, when compared with Ge, and exhibits a relatively long carrier lifetime, when compared with GaAs. RETINA SIW structures ideally require a uniform vertical distribution of photo-induced plasma. Therefore, for the same optical illumination wavelength, a relatively low absorption coefficient is needed. These features make HRS suitable for RETINA structures. Other, even more suitable materials may exist, but the search to find these is beyond the scope of this paper. For this reason, only HRS will be considered further.

The ITO layer is formed by doping In_2O_3 with Sn (In_2O_3:Sn). ITO has a plasma frequency of between 159 and 318 THz (i.e., corresponding to wavelengths of 1.887 µm to 943 nm), depending on sheet resistivity [24]. Also, ITO normally has an optical transmittance and dc electrical resistivity of 82% at an optical illumination wavelength $\lambda_{opt} = 808\,\text{nm}$ and $10^{-4}\,\Omega\cdot\text{cm}$, respectively [25]. Moreover, it has a refractive index $n \approx 1.96$ [26] and direct optical band gap ranging from 3.5 to 4.0 eV [24]. With the former, ITO can act as an anti-reflection coating (ARC) layer for the HRS substrate with theoretical thicknesses of $(1 + 2u)\,\lambda_{opt}/(4\,n)$, where $u \in [0, 1, 2, 3, \ldots]$.

2.2. Standard Analytical Plasma Profile Analysis

As illustrated in Fig. 2, the photo-induced plasma distribution is in three-dimensions. The vertical profile of excess photo-induced carriers is defined by the carrier density $N(y)$ along the y-direction. The horizontal profile is denoted by $N(x)$ along the x-direction. This assumes that there are no x-z plane spreading effects.

In the case of continuous wave (CW) or quasi-CW optical illumination, the vertical profile of a photo-induced plasma can be expressed by the following well-known expressions [13, 20, 21]:

$$N(y) = \frac{\Delta N_o}{\left(1 - \alpha_\lambda^2 L_a^2\right)} \cdot \left[e^{-\alpha_\lambda y} - \left(\frac{\alpha_\lambda L_a^2 + \nu_s \tau_L}{L_a + \nu_s \tau_L}\right) e^{-y/L_a}\right] \tag{1}$$

where $\Delta N_o = (1 - R)\cdot\frac{P\,S_\lambda\,\alpha_\lambda\,\lambda_{opt}\,\tau_L}{h\;cA}$; $L_a = \sqrt{D_a \tau_L}$; $D_a = (\mu_n + \mu_p)\cdot\frac{kT}{e}$. Therefore, the vertical distribution of photo-induced conductivity is

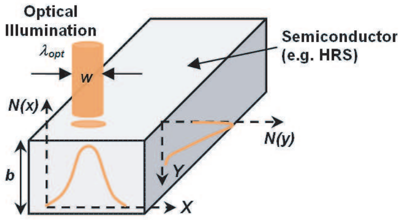

Figure 2. Photo-induced plasma distribution inside the semiconductor from single-sided illumination with a circular spot.

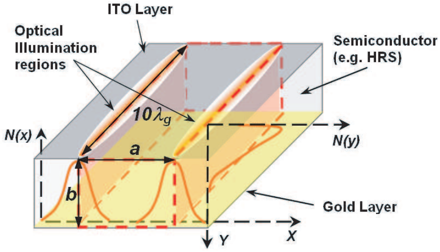

Figure 3. Illustration of a $10\lambda_g$ long RETINA SIW with single-sided illumination.

given by:

$$\sigma(y) = \Delta\sigma_o \cdot \frac{N(y)}{\Delta N_o} \tag{2}$$

where $\Delta\sigma_o = e\,(\mu_n + \mu_p) \cdot \Delta N_o$

These equations assume that μ_n, μ_p andτ_L are effectively independent of photo-induced carrier density. From (2), one can find that the maximum bulk dc photoconductivity in the vertical distribution as:

$$\sigma_{mv} = \frac{\Delta\sigma_o}{(1+\alpha_\lambda L_a)} \cdot \left[\frac{1}{\alpha_\lambda L_a}\left(\frac{\alpha_\lambda L_a^2 + \nu_s\tau_L}{L_a + \nu_s\tau_L}\right)\right]^{\frac{-\alpha_\lambda L_a}{1-\alpha_\lambda L_a}} \tag{3}$$

where, $\sigma_{mv} = 3,271\,\mathrm{S/m}$ for $\lambda_{opt} = 808\,\mathrm{nm}$ at a depth of $14\,\mu\mathrm{m}$ in HRS. With the origin of x at beam centre, the horizontal distribution of photo-induced conductivity is given by [20]:

$$\sigma(x) = \sigma_h \cdot \left[1 - e^{-w/2L_a} \cdot \cosh\left(x/L_a\right)\right] \quad \text{for} \quad 0 \le x \le w/2 \tag{4}$$

$$\sigma(x) = \sigma_h \cdot \left[e^{-x/L_a} \cdot \sinh\left(w/2L_a\right)\right] \quad \text{for} \quad w/2 \le x \le \infty \tag{5}$$

For this case, to preserve the law of conservation of charge, it is found that a value of $\sigma_h = 7,422\,\mathrm{S/m}$ is needed to give a maximum bulk dc photoconductivity in the horizontal distribution of 2,921 S/m, at P_1, for $\lambda_{opt} = 808\,\mathrm{nm}$ at a depth of $30\,\mu\mathrm{m}$ in HRS.

2.3. First-order RETINA SIW Structure Calculations

Figure 3 shows how photo-induced carriers can effectively create both *virtual* sidewalls within a HRS substrate. Conducting materials (e.g., ITO or gold) are still needed to complete the top and bottom of the RETINA SIW.

The RETINA SIW shown in Fig. 3 has been designed for an arbitrary operating frequency $f_o = 300\,\mathrm{GHz}$. The ideal internal width dimension a for this HRS-filled SIW should be such that its cut-off frequency $f_c = f_o/1.95 = 154\,\mathrm{GHz}$ for minimal loss without over-sizing. The frequency-dependent relative permittivity for HRS is $\varepsilon_r = 11.684$ at 200 GHz and 11.682 at 300 GHz [27]. Therefore, the unguided wavelength in HRS is $\lambda_{o\_HRS} \cong 293\,\mu\mathrm{m}$ at 300 GHz and the ideal internal width dimension is given by:

$$a = \frac{c}{2 \cdot \sqrt{\varepsilon_r} \cdot f_c} = 285\,\mu\mathrm{m} \tag{6}$$

The ideal lossless guided wavelength is given by:

$$\lambda_g = \frac{\lambda_{o\_HRS}}{\sqrt{1 - \left(\frac{\lambda_{o\_HRS}}{\lambda_c}\right)^2}} = \frac{\lambda_{o\_HRS}}{\sqrt{1 - \left(\frac{f_c}{f}\right)^2}} = 342\,\mu\mathrm{m} \tag{7}$$

where $\lambda_c = 2a$ is the ideal lossless cut-off wavelength.

2.4. Optical Illumination Wavelength and Power

The standard analytical analysis in Section 2.2 assumes that there are no ITO and gold layers. For more realistic modelling, a commercial

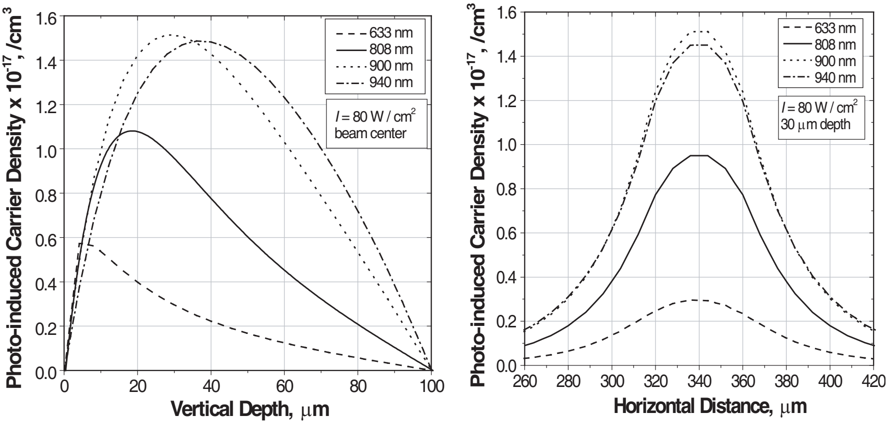

(a) (b)

Figure 4. Numerical simulation results of photo-induced carrier density for different wavelengths at 80 W/cm^2 using *Silvaco*$^{\text{TM}}$ TCAD: (a) vertical distribution, (b) horizontal distribution.

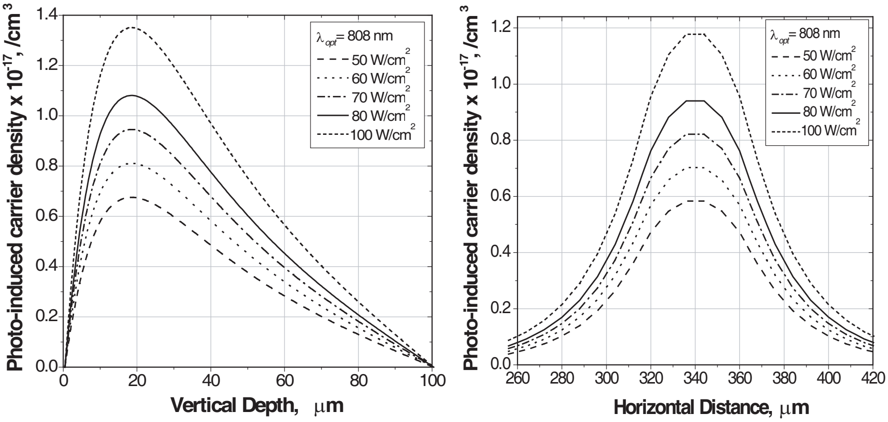

(a) (b)

Figure 5. Numerical simulation results of photo-induced carrier density for different illumination power densities at 808 nm using *Silvaco*$^{\text{TM}}$ TCAD: (a) vertical distribution, (b) horizontal distribution.

optoelectronic simulation software package (*Silvaco*$^{\text{TM}}$ TCAD [28]) was used. As a result, with HRS sandwiched between ITO and gold layers, different optical wavelengths and power densities were investigated. As seen in Figs. 4 and 5, under the same optical illumination power density $I = 80\ \text{W/cm}^2$, the 940 nm wavelength source gives the highest photo-induced charge carrier density (electrons and holes). However, 808 nm may be preferred in practice, because low-cost high power laser diodes are available at this wavelength. Therefore, for a quarter-wavelength ARC, either 103, 309 or 515 nm thick layers of ITO can be employed for an 808 nm optical source. With basic single-sided illumination, the bottom layer of the waveguide can be gold.

2.5. Photo-induced Plasma Profile Approximation

Since the spatial profiles of the photo-induced regions are relatively complicated, it is appropriate to extract quantised distributions for subsequent electromagnetic analysis. One way of doing this is to divide the whole photo-induced plasma region into several sub-regions, as shown in the Fig. 6, for CW mode optical illumination. Each sub-region has an approximate value. For example, to provide sufficient resolution without having too many regions, the cross-sectional x-y plane plasma profile was divided up into a 7×7 matrix. This number of sub-regions can vary, depending on the minimum acceptable error, choice of substrate (i.e., material and thickness), optical source (i.e., wavelength, power density and beam profile), surface conditions and structural features. However, as the diffusion length of the carriers increases with a longer carrier lifetime, seen in (1), errors from the assumption of having a homogenous photoconductivity within a sub-region will increase. As shown in Fig. 6, it is found that an improved accuracy is obtained when the sub-regions are not equally sized in the vertical direction.

With a CW optical source, using the dotted line data in Fig. 6 — dc photoconductivity σ_o extracted from *Silvaco*$^{\text{TM}}$ TCAD — and (9), it is a simple task to calculate the equivalent photoconductivity σ' profile up to THz frequencies. Also, using the solid line data in Fig. 5 and (11), the corresponding real parts of the photo-induced relative permittivities ε_r' can be calculated, as shown in Fig. 7 for 300 GHz. This information can then be divided into multiple columns and rows, so that a *virtual* MPRWG SIW can be modelled using a commercial 3D electromagnetic simulation software package [12].

As seen in Figs. 6 and 7, seven-level partitioning is performed in both vertical and horizontal directions within the 100 μm thick HRS. The frequency-dependent complex conductivity due to photo-induced carriers is given by:

$$\sigma(\omega) = \frac{\sigma_o}{1 + j\omega\tau} \equiv \sigma'(\omega) - j\sigma''(\omega) \tag{8}$$

where

$$\sigma'(\omega) = \frac{\sigma_o}{1 + \omega^2\tau^2}; \quad \sigma''(\omega) = \frac{\sigma_o \cdot \omega\tau}{1 + \omega^2\tau^2} \tag{9}$$

where,

$$\sigma_o \sim Ne(\mu_n + \mu_p) = \frac{Ne^2\tau}{\overline{m}^*} \quad \text{and} \quad \tau \sim \frac{\overline{m}^*(\mu_n + \mu_p)}{e}$$

The photo-induced plasma gives an equivalent complex relative permittivity given by [16, 23, 29]:

$$\varepsilon_r(\omega) = \varepsilon_{ro} + \frac{\sigma(\omega)}{j\omega\varepsilon_o} \equiv \varepsilon_r'(\omega) - j\varepsilon_r''(\omega) \tag{10}$$

where,

$$\varepsilon_r'(\omega) = \varepsilon_{ro} - \frac{\omega_p^2}{\omega^2 + \omega_\tau^2}; \quad \varepsilon_r''(\omega) = \frac{\omega_\tau}{\omega} \cdot \frac{\omega_p^2}{\omega^2 + \omega_\tau^2}$$

$$\omega_\tau = \frac{1}{\tau}; \quad \omega_p \sim \sqrt{\frac{Ne^2}{\overline{m}^*\varepsilon_o}} = \sqrt{\frac{\sigma_o}{\tau\,\varepsilon_o}}; \tag{11}$$

At low frequencies, the photo-induced carriers will not affect the real part of the complex relative permittivity. However, at high frequencies

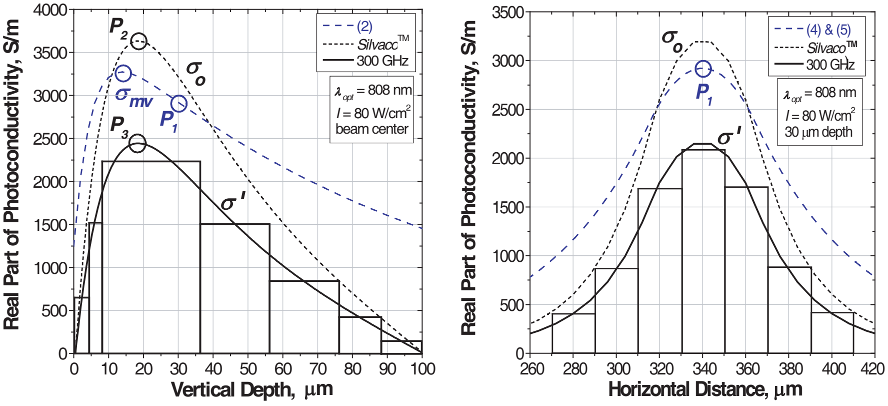

(a) (b)

Figure 6. Conversion of carrier densities (from solid line data in Fig. 5) into photoconductivity at 300 GHz and their quantization: (a) vertical distribution, (b) horizontal distribution.

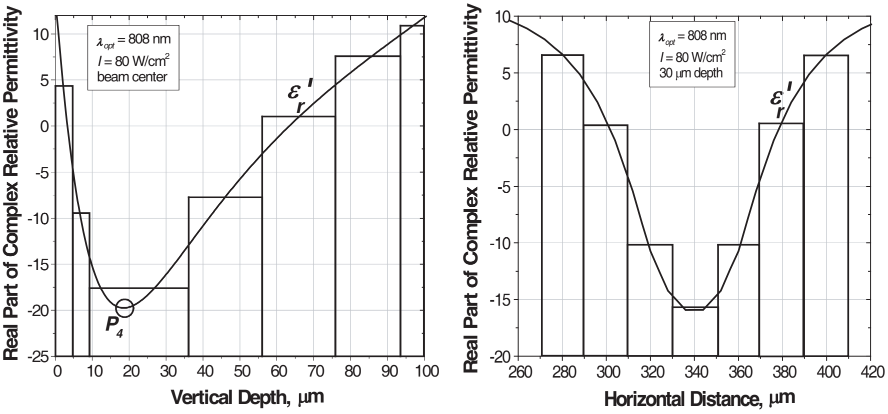

(a) (b)

Figure 7. Conversion of carrier densities (from solid line data in Fig. 5) into relative permittivity at 300 GHz and their quantization: (a) vertical distribution, (b) horizontal distribution.

(e.g., above *circa* 100 GHz), the effect of the photo-induced plasma on the real part of the complex relative permittivity can no longer be neglected. As shown in Fig. 8(a), for a peak photoconductivity of $\sigma_o = 3,631\,\mathrm{S/m}$, at point P_2, found at a depth of 19 μm with *Silvaco*$^{\mathrm{TM}}$ TCAD, as frequency increases the real part of complex photoconductivity decreases. The corresponding real part of the complex photo-induced effective relative permittivity is shown in Fig. 8(b); this increases with frequency.

It should be noted that the commercial 3D electromagnetic simulation software package HFSS$^{\mathrm{TM}}$ (versions 10, 11 & 12) assumes the classical skin-effect model, by default, to describe frequency dispersion within a good conductor at room temperature; while giving the option to input frequency-dependent values for the accurate classical relaxation-effect model [30]. However, while HFSS$^{\mathrm{TM}}$ (versions 10, 11 & 12) allows complex value entry for both conductivity and relative permittivity, only their real parts are used in calculations. As a result, the imaginary part of the complex photoconductivity should be converted into the real part of the complex relative permittivity [30]. Unfortunately, even this solution does not work with HFSS$^{\mathrm{TM}}$ (versions 10, 11 & 12), because the real part of relative permittivity is ignored when high values of conductivity are entered. In such cases, the results generated correspond to the simple relaxation-effect model [30]. Fortunately, below *circa* 500 GHz, the errors produced from this overly-simplified model will be small.

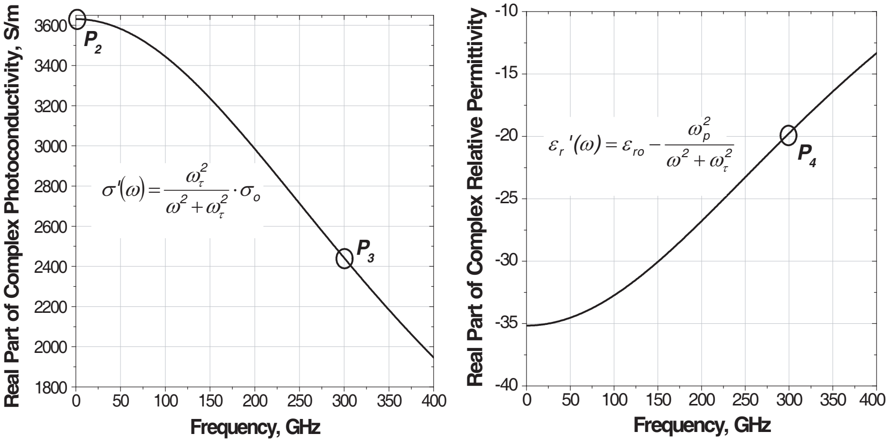

(a) (b)

Figure 8. Real parts of frequency-dependent parameters entered into HFSS$^{\mathrm{TM}}$ for $\sigma_o = 3,631\,\mathrm{S/m}$: (a) photoconductivity, (b) relative permittivity.

3. COMPLETE RETINA SIW SIMULATIONS

Using the quantized parameter values from the previous section, Fig. 9 shows the construction of a simple RETINA SIW structure in HFSS$^{\mathrm{TM}}$. Here, 8 kΩ·cm HRS is used, having a dielectric constant and loss tangent of 11.682 and 0.0006, respectively, at 300 GHz [27], with $\sim 0.5\,\mu\mathrm{m}$ thick upper ITO layer and a $1\,\mu\mathrm{m}$ thick bottom gold layer. The length of this RETINA SIW is 3.38 mm, corresponding to 10 guided wavelengths in HFSS$^{\mathrm{TM}}$.

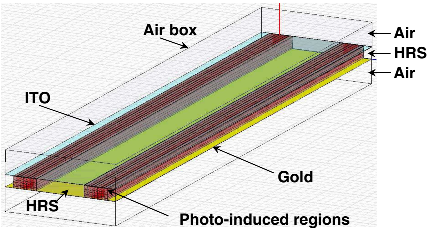

Figure 9. Isometric view of a simple RETINA SIW structure in HFSS$^{\mathrm{TM}}$.

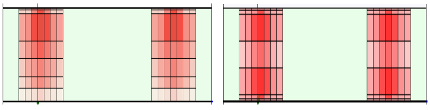

(a) (b)

Figure 10. Partitioned photo-induced regions for RETINA SIW cross-section in HFSS$^{\mathrm{TM}}$: (a) single sided, (b) double sided.

As shown in Fig. 10, the RETINA SIW structure can be formed by either single-sided illumination (projected onto the top surface), or double-sided illumination (projected symmetrically onto both top and bottom surfaces) at the same time. Fig. 11 shows a comparison of the resulting electric field distributions for each case.

The combined optoelectronic-electromagnetic simulation results for a $10\lambda_g$ long RETINA SIW are given in Fig. 12. Insertion loss with single-sided illumination is $1.35\,\mathrm{dB}/\lambda_g$ at 300 GHz. While the real part of the wall conductivity decreases with increasing frequency, as with a conventional MPRWG of fixed cross-sectional dimensions, overall attenuation still decreases with increasing frequency. This improves only slightly to $1.31\,\mathrm{dB}/\lambda_g$ at 300 GHz with double-sided illumination; however, as will be seen in the next section, this approach is needed for RETINA SIW cavity resonators.

Table 3 gives a loss comparison for various SIW technologies cited in the open literature. It can be seen that a very crude attempt has been made to frequency scale the results to 300 GHz, by assuming that attenuation due to conductivity is proportional to the square root of frequency, that dielectric losses are frequency invariant and that the dominant waveguide modes have no frequency dispersion characteristics. It should be stressed that, even though the predicted RETINA SIW loss is currently higher than other reported SIW technologies, real-time tuneable/reconfigurable operation is the real

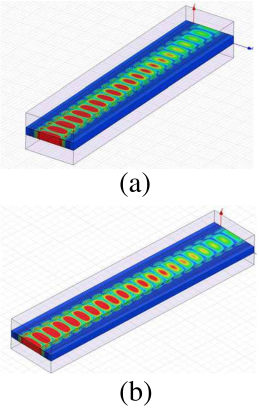

Figure 11. HFSS$^{\mathrm{TM}}$ electric field distributions for $10\lambda_g$ long RETINA SIW at 300 GHz: (a) single sided, (b) double sided.

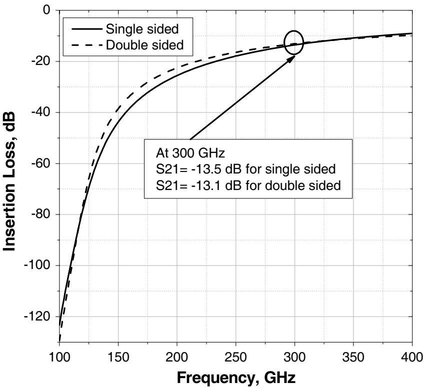

Figure 12. HFSS$^{\mathrm{TM}}$ simulation comparison of RETINA SIW waveguides ($10\lambda_g$ in length at 300 GHz) for single- and double-sided illuminations.

advantage of the RETINA technology. Indeed, loss comparison with a conventional SIW technology can be considered irrelevant, because they do not have the important advantage of being able to performance the operations of real-time tuneability or reconfigurability. Moreover, while being in its infancy, it is believed that there is a wide range of possible ways to improve the current loss performance of this RETINA technology.

Table 3. Loss comparison for various non-tuneable/reconfigurable SIW technologies.

Ref.	Technology	Frequency (GHz)	Insertion loss (dB/mm)	Conductor loss scaling to 300 GHz (dB/mm)
[31]	Alumina SIW	50	0.03	0.07
[33]	Ceramic (HT1000) SIW	60	0.20	0.45
[32]	Ceramic (QM44F) SIW	74	0.70	1.41
[34]	Polyimide (Kapton HN) SIW	79	0.17	0.33
[8]	Photoimageable Dielectric HD1000-filled MPRWG	83	1.2	2.3
[3]	Air-filled MPRWG	100	0.01	0.017
[4, 5]	Polyimide-filled MPRWG	105	8.98	15.18
[35]	Air-filled MPRWG	400	0.086	0.074
Here	RETINA (simulated)	300	3.88	3.88

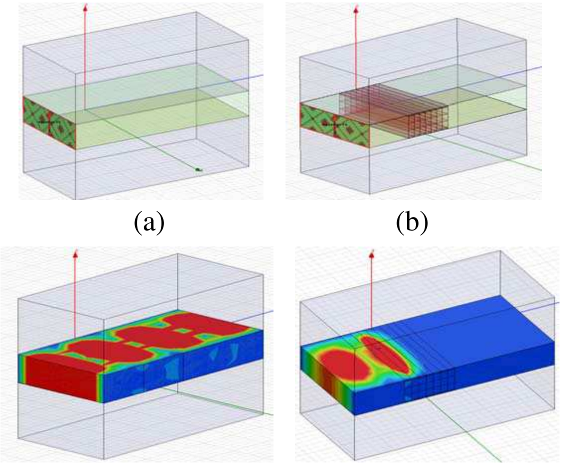
(a) (b)
(c) (d)

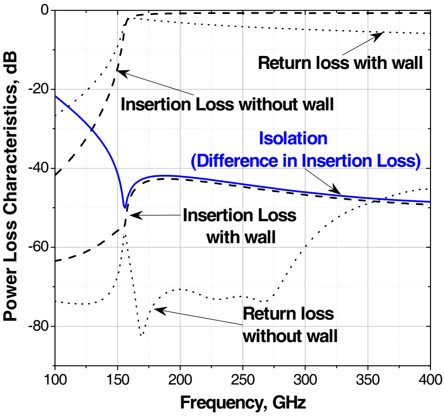

(e)

Figure 13. Transverse RETINA wall modelling with double-sided illumination: (a) HRS-filled waveguide with lossless metal sidewalls; (b) *virtual* wall inserted, (c) electric field plot for the structure in (a), (d) electric field plot for the structure in (b), (e) attenuation and isolation characteristics for the structures in (a) and (b).

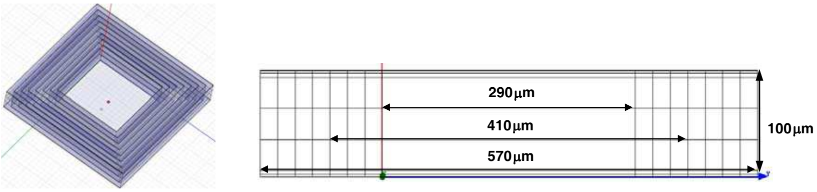

(a) (b)

Figure 14. Square RETINA SIW cavity resonator in HFSS$^{\text{TM}}$: (a) isometric view, (b) cross-section.

It is important to be able to characterize the electromagnetic boundary of a RETINA wall. To this end, Fig. 13 shows the effects of inserting a transverse RETINA wall, across a HRS-filled MPRWG with lossless metal sidewalls. For single-sided illumination, using the solid line data in Fig. 5(a) with (12), it will be seen that the plasma frequency along the vertical cut-line at beam centre will vary between 41 GHz and 3 THz. Theoretically, with an ideal brick wall spectral response, a plasma frequency below the maximum frequency of operation represents a spatially-defined electromagnetic 'gap'. For the example given here, this is approximately 12% across the vertical cut line at beam centre, for the transverse RETINA wall, where the carrier concentrations are lowest (mostly at the back side). However, it was found that both isolation and return loss are improved with double-sided illumination, which effectively closes the electromagnetic 'gap' at the bottom of the wall. In Fig. 13(e), it can be seen that at 300 GHz the wall implemented with double-sided illumination has an isolation of 46 dB and return loss of 4.8 dB. While the high isolation transverse RETINA wall absorbs a high proportion of incident power, in its non-optimum form, a significant amount of reflected power is still observed. Therefore, it can be concluded that a RETINA SIW structure is suitable for confining the dominant TE_{10} mode of propagation.

4. COMPLETE RETINA SIW CAVITY SIMULATIONS

The same RETINA SIW simulation methodology has been applied to a HRS-filled cavity resonator, as shown in Fig. 14, having the same width and height dimensions as used in the previous section. It was found that with single-sided illumination the unloaded quality (Q)-factor is less than unity. The solution is to employ double-sided illumination with the bottom gold metallisation being replaced by a similar ITO layer as that used for the top of the RETINA SIW cavity.

By using the Eigenmode solver, HFSS$^{\text{TM}}$ can give the complex

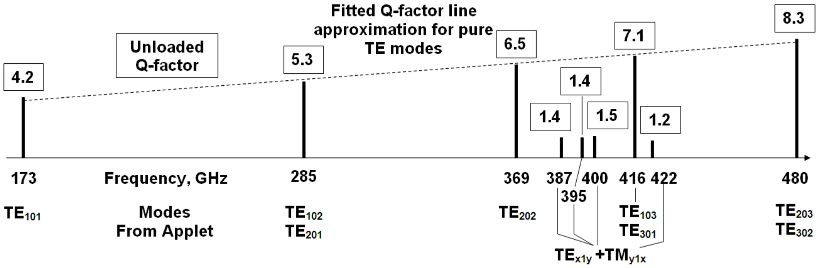

Figure 15. Double-sided illuminated square RETINA SIW cavity resonator in Fig. 14 mode spectral signature using HFSS$^{\text{TM}}$.

Table 4. HFSS$^{\text{TM}}$ eigenmode solutions for the double-sided illuminated square RETINA SIW cavity resonator in Fig. 14.

Mode	Resonant Frequency (GHz)	Unloaded Quality Factor
TE_{101}	$172.600 + j20.6487$	4.20923
TE_{201} and TE_{102}	$284.679 + j26.8047$	5.33374
TE_{202}	$368.852 + j28.2601$	6.54516
TE_{301} and TE_{103}	$416.221 + j29.1453$	7.15793
TE_{302} and TE_{203}	$480.467 + j28.8706$	8.33605

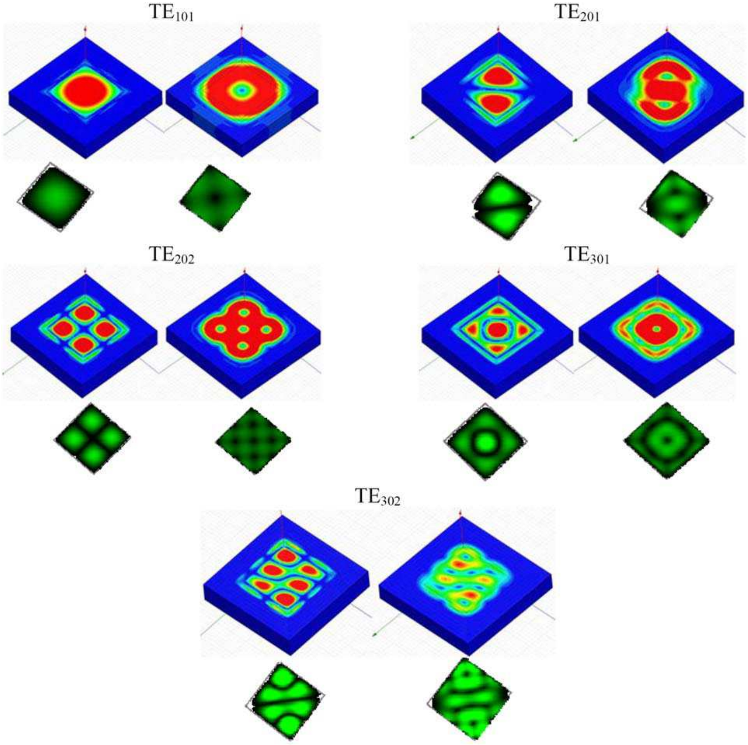

Figure 16. Electric (left) and magnetic (right) field distributions on a linear scale for the double-sided illuminated square RETINA SIW cavity resonator with corresponding modified *EMBox* field plots beneath.

resonant frequencies and associated Q-factors for each mode. With frequency-dependent material data, calculated from dc to 500 GHz, the investigation was limited to resonant transverse electric (TE) modes below 500 GHz. Table 4 lists the five lowest resonant TE modes; these were identified by modifying an online applet (*EMbox* [36]). It was first necessary to refine the available values for the cross-sectional width-to-height ratio for the cavity, by modifying the open-source applet's JAVA script. Using the modified *EMBox*, the same mode spectral signature as that found with HFSS$^{\mathrm{TM}}$ was obtained, as shown in Fig. 15.

It is easy to identify the pure TE modes, as they have relatively high Q-factors. Fig. 16 shows the electric (left) and magnetic (right) field plots for each of these modes. In addition, the corresponding field plots from the modified *EMBox* applet are shown underneath. As seen in Table 4 and Fig. 15, the Q-factors are low, even at such high frequencies, but there is a wide range of possible ways to improve this performance figure of merit.

5. CONCLUSIONS

The combined optoelectronic-electromagnetic modelling methodology for simulating RETINA SIW structures has been described in detail for the first time. While the RETINA SIW has more loss than a conventional SIW, the flexibility of being able to implement tuneable circuits and reconfigurable integrated architectures at terahertz frequencies by simply changing light patterns and in real time are very important advantages. With optimization in a wide range of associated enabling technologies considerable reductions in the predicted loss of RETINA SIW structures can be expected.

In principle, complex signal processing operations can be performed both with the use of a spatial light modulator (to efficiently create any arbitrary optical illumination pattern in the x-z plane) and directly on the carrier signal (from the tuning behaviour that results with the generation of new light patterns in real time). It is believed that, while still in its infancy, this technology could have a profound impact on the future of millimeter-wave and terahertz electronics.

ACKNOWLEDGMENT

This work was supported by the UK's Engineering and Physical Sciences Research Council (EPSRC) under Platform Grant EP/E063500/1.

REFERENCES

1. Lucyszyn, S. and I. D. Robertson, "Analog reflection topology building blocks for adaptive microwave signal processing applications," *IEEE Trans. Micro. Theory Tech.*, Vol. 43, No. 3, 601–611, Mar. 1995.
2. Lucyszyn, S., *Advanced RF MEMS*, Cambridge University Press, Cambridge, UK, ISBN-13: 9780521897716, Aug. 2010.
3. McGrath, W. R., C. Walker, M. Yap, and Y.-C. Tai, "Silicon micromachined waveguides for millimetre-wave and submillimeterwave frequencies," *IEEE Microw. Guid. Wave Lett.*, Vol. 3, No. 3, 61–63, 1993.

4. Lucyszyn, S., Q. H. Wang, and I. D. Robertson, "0.1 THz rectangular waveguide on GaAs semi-insulating substrate," *IEE Elect. Lett.*, Vol. 31, No. 9, 721–722, Apr. 1995.
5. Lucyszyn, S., D. Budimir, Q. H. Wang, and I. D. Robertson, "Design of compact monolithic dielectric-filled metal-pipe rectangular waveguides for millimetre-wave applications," *IEE Proceedings — Microwaves, Antennas and Propagation*, Vol. 143, No. 5, 451–453, Oct. 1996.
6. Lucyszyn, S., "The future of on-chip terahertz metal-pipe rectangular waveguides implemented using micromachining and multilayer technologies," *IEE Colloquium Digest on Terahertz Technology and Its Applications*, Vol. 1997, No. 151, 10/1–10/10, London, Apr. 1997.
7. Lucyszyn, S., S. R. P. Silva, I. D. Robertson, R. J. Collier, A. K. Jastrzebski, I. G. Thayne, and S. P. Beaumont, "Terahertz multi-chip module (T-MCM) technology for the 21st Century?" *IEE Colloquium Digest on Multi-chip Modules and RFICs*, 6/1–6/8, London, May 1998.
8. Aftanasar, M. S., P. R. Young, I. D. Robertson, J. Minalgiene, and S. Lucyszyn, "Photoimageable thick-film millimetre-wave metal-pipe rectangular waveguides," *IEE Elect. Lett.*, Vol. 37, No. 18, 1122–1123, Aug. 2001.
9. Stephens, D., P. R. Young, and I. D. Robertson, "Design and characterization of 180 GHz filters in photoimageable thick-film technology," *IEEE MTT-S IMS*, Vol. 1, 451–454, 2005.
10. Bowen, J. W., S. Hadjiloucas, B. M. Towlson, L. S. Karatzas, S. T. G. Wootton, N. J. Cronin, S. R. Davies, C. E. McIntosh, J. M. Chamberlain, R. E. Miles, and R. D. Pollard, "Micromachined waveguide antennas for 1.6 THz," *IEE Elect. Lett.*, Vol. 42, No. 15, 842–843, Jul. 2006.
11. Lucyszyn, S., "Substrate integrated metal-pipe rectangular waveguides," *IEEE International Microwave Symposium (IMS2010) Workshop Proceedings, WSI: Substrate Integrated Circuits*, USA, May 2010.
12. Lucyszyn, S. and Y. Zhou, "Reconfigurable terahertz integrated architecture (RETINA)," *33rd International Conference on Infrared, Millimetre, and Terahertz Waves (IRMMW-THz 2008)*, Pasadena, USA, Sep. 2008.
13. Ambroziak, A., *Semiconductor Photoelectric Devices*, Iliffe Books, London, 1968.
14. Joshi, N. V., *Photoconductivity: Art, Science and Technology*, Marcel Dekker, New York, 1990.

15. Johnson, A. M. and D. H. Auston, "Microwave switching by picosecond photoconductivity," *IEEE J. Quant. Electronics*, Vol. 11, No. 6, 283–287, Jun. 1975.
16. Lee, C. H., "Picosecond optoelectronic switching in GaAs," *Appl. Phy. Lett.*, Vol. 30, No. 2, 84–86, Jan. 1977.
17. Seeds, A. J. and A. A. De Salles, "Optical control of microwave semiconductor devices," *IEEE Trans. Micro. Theory Tech.*, Vol. 38, No. 5, 577–585, May 1990.
18. Lucyszyn, S. and I. D. Robertson, "Optically-induced measurement anomalies with voltage-tunable analog control MMICs," *IEEE Trans. Micro. Theory Tech.*, Vol. 46, No. 8, 1105–1114, Aug. 1998.
19. Platte, W., "LED-induced distributed Bragg reflection microwave filter with fibre-optically controlled change of center frequency via photoconductivity grating," *IEEE Trans. Micro. Theory Tech.*, Vol. 39, No. 2, 359–363, Feb. 1991.
20. Platte, W., "An optimization of semiconductor film thickness in light-controlled microstrip devices," *Solid-state Electron.*, Vol. 20, 57–60, 1977.
21. Platte, W., "Lichtempfindliche Halbleiterschichten in Microstrip Schaltungen," Dissertation, 78, University Erlangen-Nurnberg, 1975.
22. Flewitt, A. J. and W. I. Milne, "a-Si:H TFT thin film and substrate materials," Chapter 2 of *Thin Film Transistors: Materials and Processes, Amorphous Silicon Thin Film Transistors, Polycrystalline Silicon Thin Transistors*, Y. Kuo (ed.), 32, Kluwer Academic Pub., Feb. 2004.
23. Lee, C. H., P. S. Mak, and A. P. DeFonzo, "Optical control of millilmeter-wave propagation in dielectric waveguides," *IEEE J. Quant. Electronics*, Vol. 16, No. 3, 277–288, Mar. 1980.
24. Davenas, J., S. Besbes, and H. Ben Ouada, "NIR spectrophotometry characterization of ITO electronic property changes at the interface with a PPV derivative," *Synethetic Metals*, No. 138, 295–298, 2003.
25. Biyikli, N., I. Kimukin, B. Butun, O. Aytur, and E. Ozbay, "ITO-Schttky photodiodes for high-performance detection in the UV-IR spectrum," *IEEE J. Quant. Electronics*, Vol. 10, No. 4, 759–765, Aug. 2004.
26. Szczyrbowski, J., A. Dietrich, and H. Hoffmann, "Optical and electrical properties of r.f. sputtered indium-tin oxide films," *Phys. Stat. Sol. (a)*, Vol. 78, 243–252, 1983.

27. Afsar, M. N. and K. J. Button, "Precise millimetre-wave measurements of complex refractive index, complex dielectric permittivity and loss tangent of GaAs, Si, SiO_2, Al_2O_3, BeO, Macor and Glass," *IEEE Trans. Micro. Theory Tech.*, Vol. 31, No. 2, 217–223, Feb. 1983.
28. SILVACO, Atlas user's manual, device simulation software, 2002.
29. Dressel, M. and G. Gruner, *Electrodynamics of Solids: Optical Properties of Electrons in Matter*, Cambridge University Press, 2002.
30. Zhou, Y. and S. Lucyszyn, "HFSS$^{\text{TM}}$ modelling anomalies with THz metal-pipe rectangular waveguide structures at room temperature," *PIERS Online*, Vol. 5, No. 3, 201–211, 2009.
31. Patrovsky, A., M. Daigle, and K. Wu, "Coupling mechanism in hybrid SIW-CPW forward couplers for millimeter wave substrate integrated circuits," *IEEE Trans. Microw. Theory Tech.*, Vol. 56, No. 11, 2594–2602, Nov. 2008.
32. Henry, M., C. E. Free, B. S. Izqueirdo, J. Batchelor, and P. Young, "Millimeter wave substrate integrated waveguide antennas: Design and fabrication analysis," *IEEE Trans. Adv. Packag.*, Vol. 32, No. 1, 93–100, Feb. 2009.
33. Samanta, K. K., D. Stephens, and I. D. Robertson, "Design and performance of a 60-GHz multi-ship module receiver employing substrate integrated waveguides," *IET Microwaves, Antennas & Propagation*, Vol. 1, No. 2, 961–967, Oct. 2007.
34. Yousef, H., S. Cheng, and H. Kratz, "Substrate integrated waveguides (SIWs) in a flexible printed circuit board for millimeter-wave applications," *J. Microelectromech. Syst.*, Vol. 18, No. 1, 154–162, Feb. 2009.
35. Kirby, P. L., D. Pukala, H. Manohara, I. Mehdi, and J. Papapolymerou, "Characterization of micromachined silicon rectangular waveguide at 400 GHz," *IEEE Microw. Wireless Compon. Lett.*, Vol. 16, No. 6, 366–368, Jun. 2006.
36. http://www.falstad.com/embox/.